Effects of Spatial Energy Distribution-Induced Porosity on Mechanical Properties of Laser Powder Bed Fusion 316L Stainless Steel

Authors: Elliott Jost [a, b, 1], John Miers [a, b, 2], Aron Robbins [b, 3], David Moore [b, 4], Christopher Saldana [a,*]

[a] George W. Woodruff School of Mechanical Engineering, Georgia Institute of Technology; 801 Ferst Drive, Atlanta, GA 30332, United States

[b] Sandia National Laboratories; P.O. Box 5800, Albuquerque, NM 87185, United States

[1] ejost@gatech.edu

[2] jcmiers@gatech.edu

[3] arobbin@sandia.gov

[4] dgmoore@sandia.gov

[*] Corresponding Author: 801 Ferst Drive, Atlanta, GA 30332, United States; christopher.saldana@me.gatech.edu

Highlights

- Spatial energy density leveraged to induce different porosity distributions
- Comprehensive defect characterization used to classify defect-induced-failures
- A critical pore size was found to improve prediction of tensile loading ductility performance

Abstract

Laser powder bed fusion (LPBF) additive manufacturing (AM) offers a variety of advantages over traditional manufacturing, however its usefulness for manufacturing of high-performance components is currently hampered by internal defects (porosity) created during the LPBF process that have an unknown impact on global mechanical performance. By inducing porosity distributions through variations in print energy density and inspecting the resulting tensile samples using computed tomography, nearly 50,000 pores across 75 samples were identified. Porosity characteristics were quantitatively extracted from inspection data and compared with mechanical properties to understand the strength of relationships between porosity and global tensile performance. Useful porosity characteristics were identified for prediction of part performance. Results indicate that ductility and strain at ultimate tensile strength are the global tensile properties most significantly impacted by porosity and can be predicted with reasonable accuracy using simple porosity shape descriptors such as volume, diameter, and surface area. Moreover, it was found that the largest pores influenced behavior most significantly. Specifically, pores in excess of 125 μm in diameter were found to be a sufficient threshold for property estimation. These results establish an initial understanding of the complex defect-performance relationship in AM 316L stainless steel and can be leveraged to develop certification standards and improve confidence in part quality and reliability for the broader set of engineering alloys.

1 Introduction

Additive manufacturing (AM), the layer-by-layer creation of a part directly from a digital computer-aided design (CAD) model, is a manufacturing paradigm that is currently coming into maturity for industrial production. Despite the many well-known advantages of AM, including the ability to create complex geometries consisting of internal features which are difficult or impossible to create using traditional manufacturing methods, consolidate complex assemblies into just a few components, create functional prints, and quickly progress from design to manufacture for small-batch components, many issues persist which inhibit these advantages from being fully realized. Some of these issues include size limitations, surface roughness, low precision, and internal defects [1,2]. Qualification or certification, the process of determining the integrity of a part, must consider and account for all of these issues to safely qualify parts.

Internal defects and porosity can largely be controlled through post-processing by hot isostatic pressing (HIP) and optimization of print parameters [3–5]. However, it has been shown that these effects on performance in titanium alloys and precipitation-hardened stainless steel cannot be fully removed and thus porosity remains one of the most persistent and puzzling problems in AM research [6–9]. Consequently, the AM research community has been working to understand the role of internal defects in part performance and account for it through qualification inspections and methodologies. Qualification of additively manufactured components can take on many forms, focusing on feedstock powder [10,11], in-situ melt pool monitoring [12,13], geometric form [14], internal feature [1,2,15–17], and material properties [18], all of which inspect or monitor crucial aspects of the laser powder bed fusion additive manufacturing process. However, there currently exists a gap in model-based understanding of the effects of internal defects on global tensile performance of AM 316L SS despite the numerous studies studying porosity in this material [2,7,19–24], consequently, an inability to safely and reliably implement or qualify parts. The present research seeks to bridge this gap through statistical modeling of the complex relationship between internal defect characteristics and tensile performance metrics.

Despite the fact that most printed parts have very high bulk density (>99.9%) in their final state, pores can still have a significant impact on part performance [2,9,11]. Porosity colloquially refers to internal void-type defects caused by several different phenomena. Porosity defects, as a common issue in LPBF AM, have been the focus of many studies seeking to improve their identification for qualification purposes [25–28]. Computed tomography (CT), as a non-destructive inspection approach useful for the identification of internal features, has become the gold-standard method for porosity detection in additively manufactured components. However, standardizing the extraction of porosity data, e.g. size, shape, location, remains an area under development. For instance, researchers at the National Institute of Standards and Technology (NIST) proposed a standardized method for porosity quantification and metrology relying on Bernsen's method, a local threshold algorithm, which performed well compared to other segmentation algorithms such as Otsu's and Yen's methods [29]. However, commercial software algorithms, such as used in the current study, persist as the most common method for identification of porosity despite their general lack of transparency [30].

In LPBF AM, porosity-type defects are typically classified into three categories based on their formation mechanisms: gas pores, lack of fusion (LOF) defects, and keyhole porosity [11]. Because these categories are formed by different mechanisms they often exhibit different physical characteristics and sizes. Gas pores, by number, are the most numerous type of pore

found in AM components but are typically at the edge of detection capabilities due to the size of these defects. These small (diameter < 20 μm), spherical pores form via entrapment of gas either in the raw powder during gas atomization, or during the build process in the final part [11]. In contrast, lack of fusion defects are very tortuous in shape. These defects are formed, as the name suggests, by two melt paths or layers not fully fusing, resulting in a void. These pores are characterized by geometries containing sharp crevices and an often-elongated shape due to their orientation along build paths. Lastly, keyhole porosity is formed when localized spatial energy density is too high. This excess of energy results in partial evaporation of the metal meltpool and a subsequent formation of plasma. This causes a vapor cavity that results in entrapment of gas and therefore voids. Specifically, keyhole formation occurs when the melt pool transitions from conduction mode to keyhole mode laser melting in LPBF, which occurs when a normalized enthalpy threshold is exceeded [31]. Keyhole porosity shape is generally characterized as either spherical or long and smooth, depending on the excess of input energy, and tend to be relatively large.

While gas pore distributions in final parts are largely dictated by raw material quality, LOF and keyhole defects can be influenced and controlled to a degree by process parameter optimization [32,33]. The most often modified parameters include power, laser speed, and hatch spacing, which can be tuned to produce highly dense parts. However, defects will always be created due to small, stochastic laser power variances, recoating inconsistencies, and powder issues. Currently, aerospace standards for additively manufactured and welded components in critical applications permit porosity of up to 1.5 mm diameter in some cases [34,35]. Without model-based understanding of the relationship between defects, standards may be limited in their effectiveness, either permitting unsafe parts into service or being overly conservative in their restrictions, resulting in increased weight and costs for parts. The persistent occurrence of porosity defects means that an understanding of the effects of these defects is critical to the success of these components in critical structural applications.

Despite relatively in-depth knowledge about defect formation, the relationship between internal defects and global part performance under various loading conditions is not fully understood. Many studies have been performed in this area, but most rely on qualitative inspection of components and on generalized measurements such as total pore count and bulk density. These studies seek to understand the defect-tensile performance relationship and have covered a variety of materials including 316L SS [2,19], Ti-6Al-4V [7], and 17-4PH SS [9,17].

For example, Madison et al. [9] inspected dozens of 17-4PH tensile using CT and found relatively weak correlations between defect properties and tensile performance. This study examined porosity distribution characteristics including total number of defects, equivalent spherical diameter, volume, among others and found relatively low correlation between defects and behavior, the maximum being an R-squared (R^2) value of ~0.50. Slightly better success was had when multiple pore parameters were combined using ANOVA techniques, reaching a maximum R^2 of 0.60. Boyce et al. [17] utilized extreme value statistics to reveal failure-critical defects in 17-4PH SS subject to tensile loading. Examining over 1000 samples, this study emphasized the need of large sample set sizes for characterization of the stochastic behavior of AM materials.

In this study, to understand the complex relationship between internal defects and tensile performance, three sample arrays consisting of 25 tensile samples each were manufactured at

three different print settings designed to induce varying defect distributions. These samples were then inspected using computed tomography to systematically and quantitatively characterize the defect distributions within the samples. Samples were pulled to failure in tension, mechanical properties calculated, and the resulting fracture surfaces inspected using scanning electron microscopy (SEM). Defect feature distributions gathered from CT inspections were then analyzed and compared with mechanical properties to understand the relationship between defects and global tensile performance.

2 Methods

Three build plates were manufactured at three different global energy density (GED) conditions using an EOS M290 additive manufacturing machine equipped with a 400 W IPG Photonics Laser. The default EOS scan strategy was used, with a laser stripe width of 5 mm and an overlap of 0.12 mm. In this scan strategy, the laser traces contours around each component slice during printing to create improved surface quality on the component exterior. Additionally, a 67 degree rotation was utilized each layer to help reduce thermal warpage and the creation of anisotropy in the component. Parts were built using constant parameters and build strategy throughout the entire z-height of the build. Each sample array was printed with the axial direction of the tensile sample oriented with the z-axis (vertically), as shown in Figure 1a so as to maximize print quality, which has been shown to be well correlated with print orientation [36–38]. In this way, the present study sought to isolate the effects of pores from the effects of surface irregularities as much as possible in an as-built condition for small-scale components.

GED, a measure of spatial energy density that is often used for tuning machine parameters, can be calculated using Equation 1, where P is laser power, H is hatch spacing, and S is laser scan speed. GED is the two-dimensional equivalent of volumetric energy density, which includes laser thickness as a parameter in the denominator and is commonly used to understand AM builds. Layer thickness was kept constant at 20 μm in this study, so it can be assumed that GED and volumetric energy density would provide identical trends and only be different by a scaling factor of $1/t$ where t is layer thickness. Power was kept constant during each build and was chosen as the independent variable changed between builds due to its established impact on part quality. Power was only modified for the core parameters of the part, while contour parameters were kept at their default values. More in-depth, parametric investigation of a larger power-speed-hatch spacing space was determined to be beyond the scope of this study. Instead, the variation of laser power, reflected by the GED value, was used a means to induce different porosity distributions between the three builds. Investigation of this larger parameter space and its effects on part quality can be found elsewhere [5,39,40].

$$GED = \frac{P}{HS} \tag{1}$$

One tensile array from each of the three builds, consisting of 25 tensile dogbones with dimensions of 1 mm^2 cross-section and 4 mm gage length, was used for this study, conforming to proportions prescribed by the ASTM E8 standard [41] but linearly scaled to the desired cross-section. The small size of samples was chosen to mimic small AM features such as the struts found in lattices, which often have diameters on the order of 1mm [38]. The sample size of 75 total dogbones was determined to be sufficiently large to capture both the tensile behavior and

the statistical distribution of defects most commonly found in this type of part. GED parameters for each of the three builds are shown in Table 1.

Table 1. Print parameter summary

	P (W)	H (mm)	S (mm/s)	GED (J/mm^2)
High GED	220	0.09	1083	2.26
Nom GED	195	0.09	1083	2.00
Low GED	170	0.09	1083	1.74

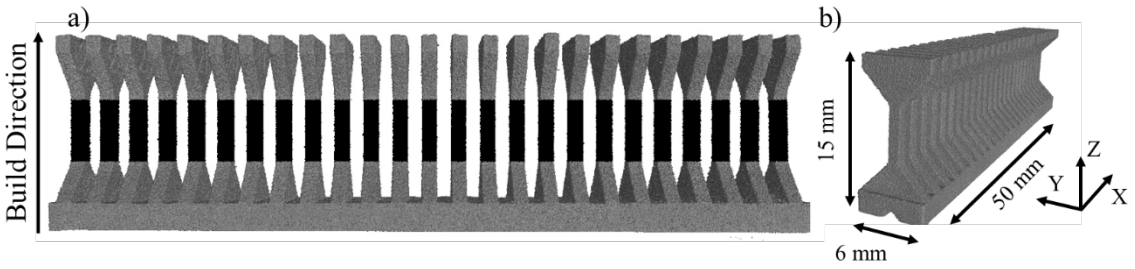

Figure 1. Test sample array CT volume. a) Array with analyzed gage sections highlighted and build direction (+Z) indicated. b) Array with dimensions and CT scan coordinate system shown at origin where the axis of the sample array is aligned with the x-axis and the axis of the sample gage sections is parallel to the z-axis.

Computed tomography (CT) inspections were performed on the sample arrays to quantitatively assess the defect distributions of the samples prior to testing. CT inspections were carried out using a Nikon M2 Dual Head 225/450 kV machine equipped with a Perkin Elmer detector. The manufacturer-recommended auto-conditioning warmup routine was performed to ensure a stable operating voltage and therefore a steady image. A helical scan path was chosen to maximize resolution of the elongated sample arrays. A helical scan effectively removes some types of imaging artifacts and allows acquisition of a single volume of elongated data [42]. This technique helps optimize the scanning of high aspect ratio parts such as the thin dogbone arrays used in the present study. A resolution of 10 µm per cubic voxel edge ($1x10^{-6}$ mm^3 voxel volume) was achieved with an acceleration voltage of 440 kV and a tube current of 198 µA. This resolution was determined to provide adequate detail for shape assessment of porosity at the size scale of interest to the authors. Prior research suggests gas pores are typically < 20 µm in diameter whereas keyhole and lack of fusion porosity are most often larger than this and also most damaging to mechanical performance [11]. Furthermore, others have suggested that pore identification requires at least 8 (2x2x2) voxels in each orthogonal direction [24,43] and that highly detailed shape assessment requires at least 125 (5x5x5) voxels [44]. While most of the defects identified in this study fall well below this 125 voxel mark, the authors contend that the pores that will be shown to be of the most consequence, those ≥125 µm diameter, are large enough to be sufficiently characterized. A 1 mm Cu prefilter was used to mitigate beam hardening interference with defect assessment. A detailed summary of CT scan parameters is presented in Table 2.

Table 2. CT Inspection Parameters

CT Parameter	Value
Acceleration Voltage	440 kV
Current	198 µA
Resolution (voxel edge)	10 µm
Number of Projections	4944
Detector Size	4000 x 4000 pixels
Binning	2 x 2 pixels
Field of View	20 x 20 mm
Pixel Pitch	200 µm
Exposure Time	1000 ms
Scan Duration	82 minutes
Beam Hardening Filter	1 mm Cu

Analysis of CT data was performed in Volume Graphics VGSTUDIO MAX 3.1, a commercial CT data analysis software. Following a surface determination using an advanced deformable surface refinement technique, CT volumes were digitally registered using best-fit geometry elements such that the volumes aligned with the coordinate system in Figure 1b. Regions of interest (ROIs) were defined using a rectangular prism to define the gage section for each sample as the same size and relative location for fair comparison of defect distributions and locations within a sample as well as to restrict analysis zones to those defects in the gage section.

To identify internal defects, VGDefX, a commercial porosity identification algorithm was used. A 2-voxel offset from the determined surface was set in combination with a medium adaptive noise reduction scheme to ensure noise or edge artifacts were not misidentified as physical defects. Using this analysis, 32 quantitative descriptors were extracted for each of the nearly 50,000 pores identified across the 75 inspected samples. For the sake of brevity, not all defect descriptors will be presented in this paper, but presented analysis will be constrained to those that offered promise as performance predictors using the approach presented in Section 3.4.

Several of the extracted defect features to be presented warrant further explanation. Diameter is calculated as that of the minimum sphere that encompasses the defect and is often referred to as the minimum bounding sphere. Compactness and sphericity both describe the shape of the defect and are defined as follows. Compactness describes the volumetric efficiency of the defect by indicating the percent volume the defect takes up in the minimum bounding sphere. Sphericity is a similar metric which compares the surface area of the defect to that of the minimum bounding sphere. Equations 2 and 3 present mathematical descriptions of compactness and sphericity used to calculate these characteristics where V is volume, d is diameter, and A is surface area.

$$Compactness = \frac{V_{defect}}{V_{sphere}} = \frac{6V_{defect}}{\pi d_{defect}^3} \quad (2)$$

$$Sphericity = \frac{A_{sphere}}{A_{defect}} = \frac{\pi d_{defect}^2}{A_{defect}} \quad (3)$$

Distance to center is the Euclidean distance between the centroid of a defect and the center of the gage section in the x-y plane, as defined by the coordinate system in Figure 1. Lastly, principal component axis (PCAx) analysis was performed on each identified defect. PCAx deviation indicates the standard deviation of the position of the voxels that describe a pore along each orthogonal PCAx, where PCAx deviation 1 corresponds to the standard deviation along the most pronounced axis of the defect volume. Standard deviations are calculated as the square roots of the eigenvalues resulting from PCAx analysis. A high PCAx deviation indicates poor alignment of the pore voxels with that axis and low ratio indicates the voxels are well-aligned. In other words, a pore with a high PCAx deviation may resemble a pancake and a low PCA deviation may resemble a thin cylinder-like crack. The PCAx maximum and minimum deviation ratios indicate the ratio between PCAx deviation 1 or 3, respectively, and the radius of the circumscribed sphere of the defect.

Following CT inspection, tensile testing of samples was performed using a custom, high-throughput tensile testing system equipped with an Interface 2-kip load cell that allows for the automated, rapid testing of tensile samples. This setup, described in more detail elsewhere [45], is capable of semi-autonomously testing 50-100 samples per hour due to a stage for sample movement and two PointGrey 5 MP digital image correlation (DIC) cameras used as automated, virtual strain-gauges. Using these cameras a spatial resolution of ~0.003 mm/pixel was achieved. A nominal field of view of 8 x 8 mm was used and images were acquired every 0.3 seconds, resulting in an average of ~300 images taken during each tensile test. Engineering strain was determined using the virtual extensometer and calculated in real time at the camera refresh rate using the Vic-Gauge software by Correlated Solutions. Sample gage section size was also calculated using the cameras to accurately calculate stress values by measuring and multiplying the thicknesses of two orthogonal sides of a sample gage section. To prepare samples for DIC measurements, samples were speckled with a white undercoat and a black speckle pattern via spray paint. Samples were pulled at a constant, quasi-static rate of 0.03 mm/s (0.0075 mm/mm/s), which is compliant with the ASTM E8 standard for tensile testing of samples with elongations greater than 5% [41].

Following mechanical testing, the resulting fracture surfaces were examined using scanning electron microscopy. Samples were imaged with an acceleration voltage of 15 kV using a Zeiss Ultra 60 Field Emission Scanning Electron Microscope (SEM) equipped with a Schottky FEG gun. The secondary electron detector was used to capture the most topographical information possible.

3 Results

3.1 Mechanical Properties

High-throughput mechanical testing resulted in tensile properties of the samples including ultimate tensile strength (UTS), strain at UTS, ductility (often referred to as elongation at fracture), modulus (obtained from unloading and reloading samples for computational simplicity), yield stress (measured from the initial loading yield), and strain at yield. Raw stress-

strain data is presented in Figure 2 and the loading/unloading curve for modulus calculation is highlighted. A summary of measured properties is presented in Table 3. In this table it can be seen that the elastic modulus, at an approximate value of 125 GPa, is well below the nominal wrought value of 193 GPa [46]. This difference can be attributed to the scale-dependent property phenomena observed in small AM components. For example, in Ref. [47] the authors measured an elastic modulus of 121 GPa for 1 mm^2 square cross-section 316L samples. In summary, a reduction of apparent material properties, specifically elastic modulus and ultimate tensile strength, can be observed as component size is decreased as a result of the increasing role of surface roughness on material response [38,47]. Furthermore, the [001] microstructural texture, aligned in the loading direction [47] as a preferential growth direction in LPBF [48,49] of the austenitic (FCC) stainless steel samples, has been shown to result in significant decreases in modulus compared to the isotropic polycrystalline value [50]. An alternative method for measurement of elastic modulus not taken here can be found in Ref. [51].

From the data in Table 3 it can be seen that, overall, variability of properties tended to be slightly higher for high GED samples compared to the nominal and low GED conditions. This is especially evident in UTS, modulus, and yield strength. The most significant differences in mechanical properties between GED types occur in UTS strain and ductility values, particularly in the high GED samples. These samples suffer a decrease in UTS strain of approximately 10% and a decrease in ductility of 12% compared to their nominal counterparts for these properties. However, variability of these properties, as measured by standard deviation, is consistent across GED conditions at approximately 2.7% and 3.7%.

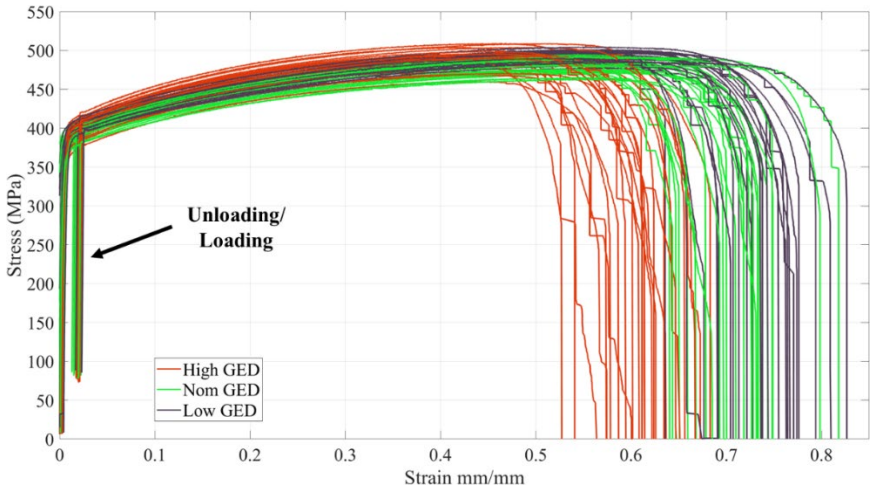

Figure 2. Stress-strain data from tensile tests.

Table 3. Experimental summary for all GED levels (mean ± population standard deviation). N = 25 for each GED condition

Mean Value	Modulus (GPa)	Yield Stress (MPa)	Yield Strain (%)	UTS (MPa)	UTS Strain (%)	Ductility (%)
High GED	127.3±3.6	337±19.0	0.469±0.015	490±13.4	45.2±2.7	60.7±3.59
Nom GED	124.3±3.2	358±18.4	0.494±0.016	481±12.9	54.5±2.7	70.9±3.68
Low GED	133.2±3.3	366±18.0	0.481±0.015	494±11.3	56.5±2.3	73.6±3.76

3.2 CT Inspection Results: Defect Characteristics

Table 4 summarizes CT inspection results for important defect parameters. This data is visualized on a normalized scale in Figure 3 in which data is scaled such that the mean value for a defect feature (e.g. diameter) across all GED conditions is equal to 1.0. As can be seen from this table and figure, samples produced in the high GED condition exhibit higher standard deviation as well as higher values at the mean and D_{90} (90^{th} percentile) values in most cases, particularly volume. Additionally, these results indicate that high GED samples tend to have defect distributions with less-uniform characteristics and larger defects overall. For example, the D_{90} pore volume is significantly larger for high GED samples compared to the nominal and low GED samples at 12.50 $x10^{-5}$, 9.79 $x10^{-5}$, and 9.12$x10^{-5}$ mm^3 for these conditions, respectively. This trend persists for other defect features, including diameter and surface area.

However, defect feature distributions are fairly consistent across GED types at the lower end (D_{10}) of distributions, such as in the case of diameter, where the high, nominal, and low GED values are 0.067, 0.065, and 0.067 mm, respectively. Differences seen in the consistency of defect features across GED types are indicators that defects at both extremes of the spectrum, particularly for size, are formed by different physical phenomena. These differences are consistent with what would be expected when observing different types of defects. Other defect feature mean values such as sphericity and compactness tend to be largely the same for each of the three GED conditions.

Table 4. Defect feature summary
High GED: N=19,542; Nom GED: N=11,632; Low GED: N=16,436

	Mean			D_{10}			D_{90}			Standard Deviation		
GED:	High	Nom	Low	High	Nom	Low	High	Nom	Low	High	Nom	Low
Global Density (%)	98.71	99.37	99.14	98.24	99.05	98.64	99.06	99.64	99.47	0.306	0.255	0.36
Diameter (mm)	0.093	0.087	0.090	0.067	0.065	0.067	0.127	0.118	0.120	0.024	0.021	0.020
Volume ($1x10^5$ mm^3)	6.581	5.431	5.231	3.040	3.040	2.700	12.50	9.790	9.120	6.463	3.118	3.074
Surface Area (mm^2)	0.015	0.013	0.013	0.010	0.010	0.010	0.030	0.020	0.020	0.009	0.007	0.006
Compactness	0.145	0.162	0.139	0.090	0.090	0.080	0.220	0.230	0.210	0.053	0.053	0.049
Sphericity	0.550	0.533	0.555	0.470	0.450	0.480	0.620	0.600	0.620	0.057	0.055	0.054
PCAx Deviation 1	0.023	0.022	0.022	0.017	0.016	0.017	0.03	0.029	0.029	0.005	0.005	0.005
PCAx Deviation 2	0.013	0.012	0.012	0.008	0.008	0.008	0.019	0.017	0.017	0.004	0.004	0.004
PCAx Deviation 3	0.007	0.007	0.006	0.004	0.005	0.004	0.01	0.009	0.008	0.003	0.002	0.002
Max. PCAx Deviation Ratio	49.12	49.98	49.96	43.27	45.03	44.9	54.70	55.20	55.1	4.544	3.901	3.970
Min. PCAx Deviation Ratio	14.42	16.47	13.56	9.29	12.41	9.28	20.26	20.64	18.53	4.395	3.294	3.862

Dist. to Center (mm)	0.349	0.330	0.340	0.150	0.138	0.148	0.532	0.513	0.517	0.144	0.142	0.140

Figure 3. Defect feature distribution summary. Data normalized such that 1.0 is the mean value of the entire defect character distribution containing all GED conditions. The filled box represents the D_{25}-D_{75} range for each GED type and the line extends from D_{10}-D_{90}. Global Density is not included because the range is very small relative to other defect features.

Figure 4 presents a representative CT inspection image of a high GED sample gage section. This figure shows the wide variety of pore sizes distributed in the high GED samples as well as pore spatial distribution throughout the sample. Defect location was considered to gain further insight into mechanisms of porosity formation observed in these samples. Figure 5 presents defect location in the x-y plane of the gage sections for all samples separated by volumetric percentile range and GED condition. This figure reveals that the largest pores, existing in the 90th percentile by volume or greater, tend to form around the edge of the samples and under the non-nominal GED conditions, particularly in the high GED condition. Pores below the 75th percentile tend to be distributed uniformly in the x-y plane and thus are not all shown.

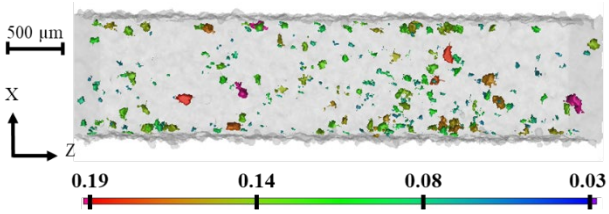

Figure 4. Semi-transparent CT volume of high GED gage section. Colorbar denotes pore diameter in mm.

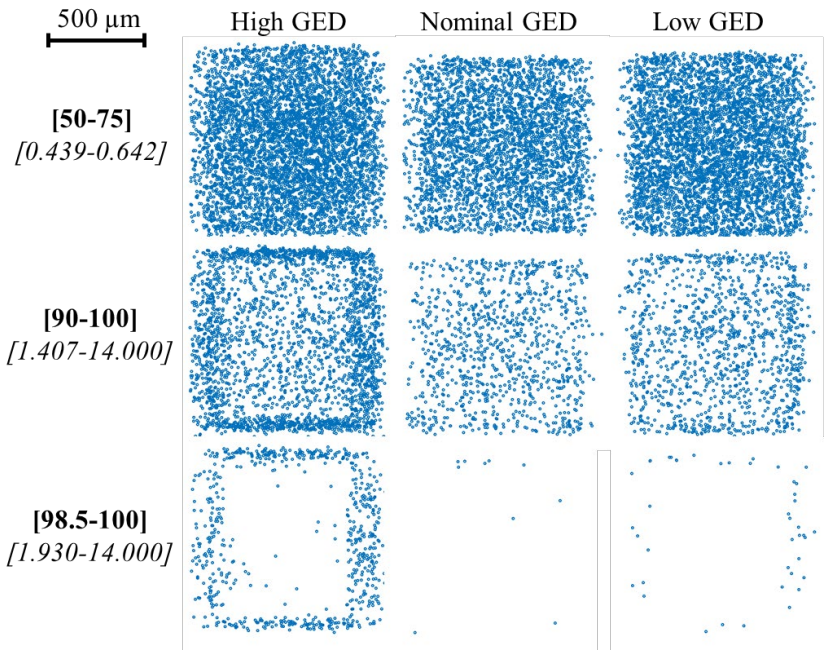

Figure 5. Pore location maps at uniform scaling for various percentiles for each GED condition. Data points indicate only location. Bold bracketed numbers in leftmost column indicate percentile value. Volume values are shown in italics and brackets in units of $1x10^{-4}$ mm^3.

Distance to center results for the various volumetric percentile ranges and GED types are presented in Table 5. As can be seen from this table, average defect distance to center in the x-y plane increases with increasing defect volume while standard deviation decreases. This trend is particularly strong in the high GED samples, where average distance to center increases from 0.349 mm in the 0-100 volumetric percentile range to 0.457 mm in the 98.5-100 percentile range. This trend of increasing distance to center with increasing pore size can be seen most clearly in Figure 6, which shows the mean distance to center of pores in each volumetric percentile range listed in Table 5. In this figure, the mean distance to center is shown to be approximately the same across ranges up to the 75th percentile. However, a sharp increase begins after this 75th percentile mark, especially for the high GED condition.

Table 5. Mean value +/- standard deviation (mm) of pore distance to gage center at various volumetric percentile ranges.

Volume Percentile	High GED	Nominal GED	Low GED
All Pores: 0-100	0.349 ± 0.144	0.330 ± 0.142	0.340 ± 0.140
0-25	0.336 ± 0.141	0.326 ± 0.140	0.335 ± 0.138
25-50	0.333 ± 0.142	0.326 ± 0.142	0.332 ± 0.138
50-75	0.337 ± 0.144	0.332 ± 0.142	0.340 ± 0.139
75-100	0.381 ± 0.143	0.338 ± 0.143	0.352 ± 0.142
90-100	0.416 ± 0.132	0.346 ± 0.144	0.360 ± 0.144
98.5-100	0.457 ± 0.093	0.419 ± 0.138	0.446 ± 0.078

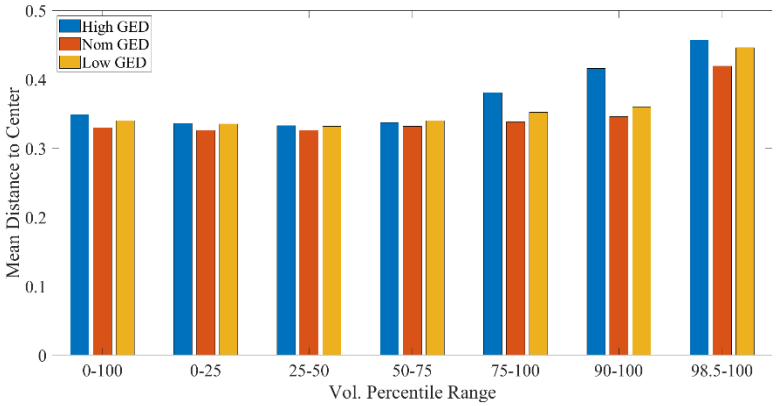

Figure 6. Mean pore distance to gage center as a function of volumetric percentile.

3.3 SEM Inspection

Representative fracture surface images from each GED condition are shown in Figure 7. Defects seen on the fracture surfaces are highlighted in green to aid in visualization. As can be seen from these few images, trends observed in CT data regarding pore size and location for each GED type are also observed in SEM images. Specifically, large pores occur around the edges and appear to be most common in the high GED samples, while low GED samples have very small pores occurring in no obvious spatial pattern. This phenomena has also been observed in AM 316L SS elsewhere [2].

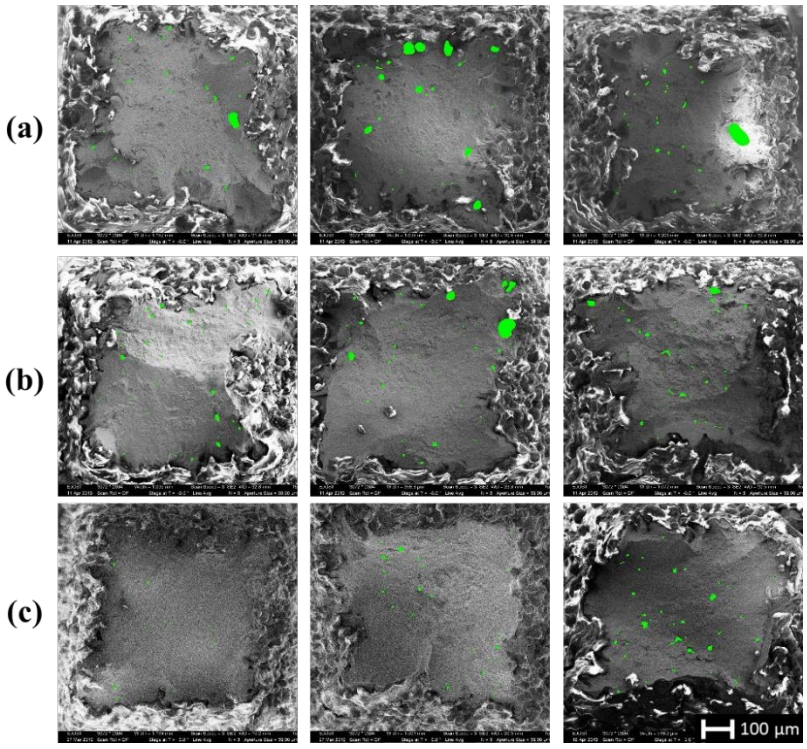

Figure 7. Select fracture surface SEM images with overlays of identified porosity. a) High GED, b) Nominal GED, c) Low GED

3.4 Defect-Property Correlations

To better understand the relationship between defects and global mechanical properties, these properties were plotted against each other and statistical relationships were quantitatively valued to identify key defect features indicative of changes in mechanical performance. One defect feature datapoint was created for each sample by using the mean value of the property of all pores considered in that sample and plotted against the mechanical properties of the sample. These relationships were quantified using a coefficient of determination (R^2) method resulting from a linear least squares curve fit. A statistical test was used to determine whether correlations were statistically significant.

The coefficient of determination, often referred to as the R^2 value, is an indicator of how well a model, in this case a linear model, represents the data used to create the model. R^2 values were calculated for all identified defect and mechanical property relations. A linear least squares regression fit was chosen as the model because it allows for simple comparison of the 100+ relationships analyzed in this study. More complex models such as quadratic or cubic could potentially mask relationships and make it more difficult to isolate porosity characteristics that strongly influence mechanical behavior. Using this first-order model, defect features that impact mechanical performance can be rapidly identified and follow-up studies can be designed to further understand the likely-more-complex relationship of an individual defect feature and its effects on mechanical properties. Furthermore, a statistical p-value was calculated from the linear model, which indicates the probability that the results observed occurred due to a true relationship between two variables, assuming the null hypothesis is correct. A p-value of 0.05 or less was chosen as the acceptance criterion for these tests, which indicates a ≥95% confidence in the observed results.

Figure 8 presents R^2 results for all relationships considered using the mean property of that sample. Of the considered mechanical properties, strain at UTS, ductility, and modulus appear to be related to defect characteristics. Most notably, volume, surface area, and maximum principal component axis deviation ratio (Max. PCAx Dev. Ratio) have the strongest correlations with strain at UTS and ductility of the considered properties with R^2 values in the range of 0.46-0.52. Table 6 presents the p-values for each individual relationship shown in Figure 8. Relationships that were shown to be statistically significant are shown in boldface. However, R^2 values less than 0.5 are generally considered to be very weak correlations and do not indicate a strong relationship that would allow for defects to serve as reliable predictors of performance metrics. To improve upon the weak relationships observed when considering all detected defects in a sample, the same relationships were calculated when only considering pores larger than a particular threshold. To accomplish this, an initial criterion of a defect being ≥150 μm in diameter allows for significantly better correlation strength to be resolved. It should be noted that by filtering the pores to be considered in the analysis, the number of pores considered in any individual sample drops significantly. Two samples without pores larger than the specified size threshold were not considered in this analysis.

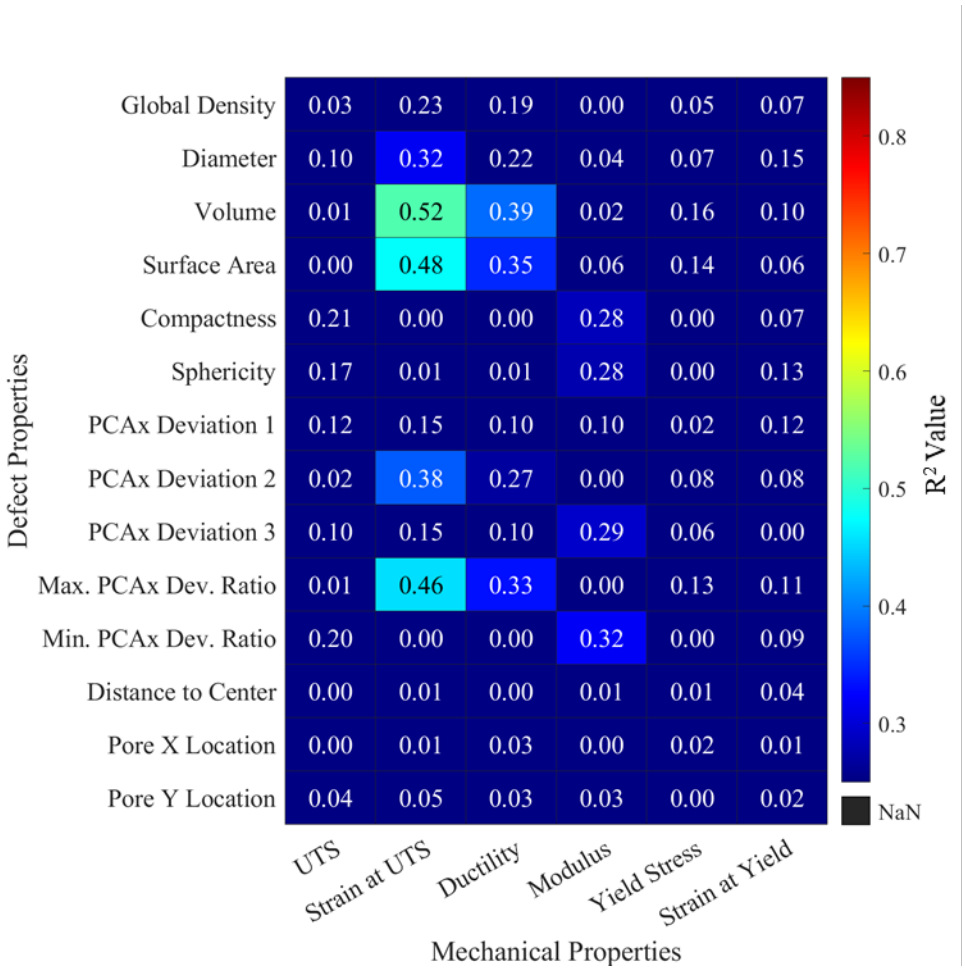

Figure 8. R^2 value heatmap comparing defect features and mechanical properties. All defects considered.

Table 6. Truncated defect-property relationship p-values with statistically significant relationships in boldface

	UTS	Strain at UTS	Ductility	Modulus	Yield Stress	Strain at Yield
Global Density	0.121	**0.000**	**0.000**	0.759	0.052	**0.021**
Diameter	**0.007**	**0.000**	**0.000**	0.072	**0.022**	**0.000**
Volume	0.489	**0.000**	**0.000**	0.239	**0.000**	**0.005**
Surface Area	0.917	**0.000**	**0.000**	**0.042**	**0.000**	**0.042**
Compactness	**0.000**	0.594	0.780	**0.000**	0.712	**0.017**
Sphericity	**0.000**	0.348	0.339	**0.000**	0.673	**0.001**
PCAx Deviation 1	**0.002**	**0.000**	**0.007**	**0.004**	**0.179**	**0.002**
PCAx Deviation 2	0.253	**0.000**	**0.000**	**0.961**	**0.014**	**0.015**
PCAx Deviation 3	**0.005**	**0.000**	**0.004**	**0.000**	**0.031**	0.548
Max. PCAx Dev. Ratio	0.333	**0.000**	**0.000**	0.555	**0.001**	**0.004**
Min. PCAx Dev. Ratio	**0.000**	0.754	0.789	**0.000**	0.787	**0.008**
Distance to Center	0.739	0.328	0.623	0.299	0.368	**0.076**
Pore X Location	0.769	0.326	0.149	0.833	0.206	0.366
Pore Y Location	0.082	0.067	0.143	0.136	0.708	0.284

As seen in Figure 9, consideration of only the largest pores in a sample, those over 150 µm in diameter, serves as a significantly better predictor of performance than does consideration of all pores. In general, relationships that were already strong were shown as strengthened by using this method. Specifically, size descriptors such as diameter, volume, surface area, and projected size, increased significantly for ductility and strain at UTS. Pore volume continues to be one of the best indicators for strain at UTS and ductility performance, having R^2 values of 0.67 and 0.53, respectively. Based on the results presented here, the authors propose that diameter, volume, or surface area serve as the best indicators for component qualification inspection purposes. As with consideration of all pores, UTS, modulus, and yield stress properties show no correlation with defect characteristics.

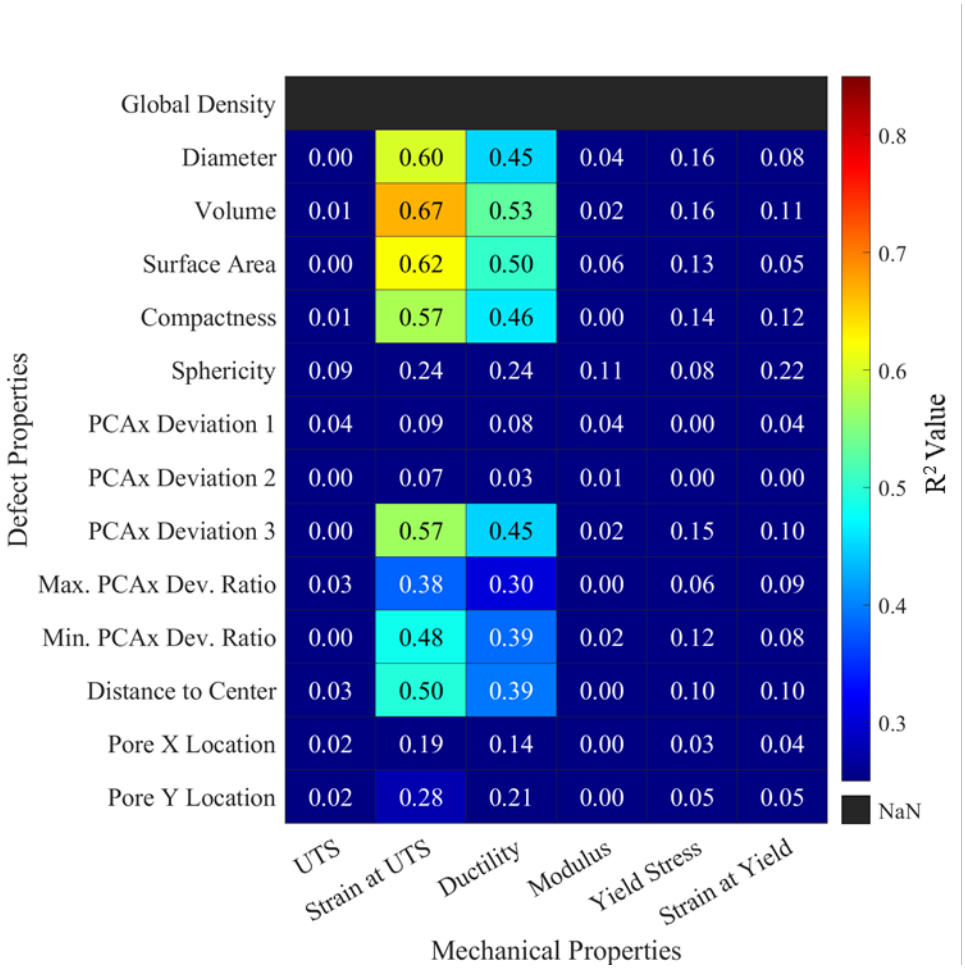

Figure 9. R^2 value heatmap comparing defect features and mechanical properties. Defects > 150 µm in diameter considered.

Due to the increase in R^2 values when only considering pores larger than 150 µm shown in Figure 9, it is implicit that a minimum defect size threshold exists that is optimal to predict tensile performance metrics. To investigate this size threshold, an optimization study was performed in which various diameter thresholds for considered pores were used to calculate R^2 values as in Figure 8 and Figure 9. Using minimum pore diameters from 50-200 µm, R^2 values were calculated, the results of which are shown in Figure 10.

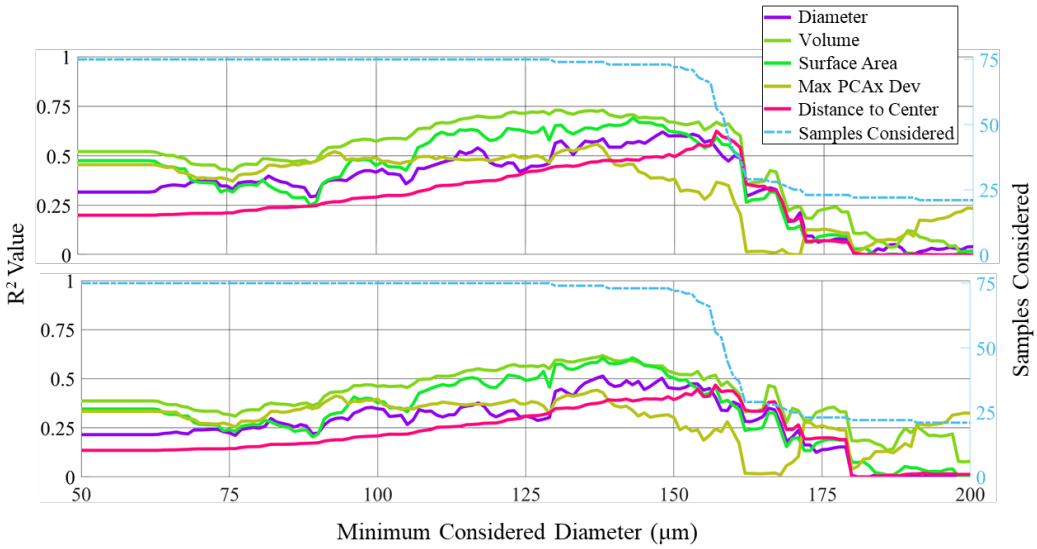

Figure 10. R^2 value as a function of minimum considered diameter for a) Strain at UTS and b) Ductility.

As can be seen in Figure 10, as minimum diameter considered in analysis increases, the R^2 value generally increases for considered defect features for strain at UTS and ductility, which is shown by the positive trend in the plotted lines until approximately 160 µm. R^2 values peaking for many defect features at ~0.65-0.75 when 130-135 µm is used as the minimum considered diameter threshold, showing only the most important defect property data. After approximately 160 µm, the R^2 values tend to decrease. This is hypothesized to be due to the fewer number of samples that are considered after this point, shown by the dashed line in this figure. Samples considered decreases because samples without pores in the specified range were not considered.

4 Discussion

The data presented in this study provide promising results for the establishment of qualification metrics and inspection thresholds for thin-walled additively manufactured 316L stainless steel components subject to tensile loading conditions.

4.1 Keyhole Porosity

With trends identified that relate defect features to global mechanical properties, the cause of the defects in this study must be considered to mitigate impacts on performance in future components. Location maps generated from computed tomography data shown in Figure 5 highlight trends relating pore volume and location. From the subfigures showing location of pores for various ranges of volumetric percentiles as well as the data provided in Table 5 and visualized in Figure 6, it is clear that the largest pores tend to form around the sample boundaries, whereas the smallest pores form uniformly throughout the sample. It is anticipated that the smaller pores are gas pores and will thus need to be mitigated through the use of higher quality powder. For example, plasma rotating electrode processed (PREP) powders have been shown to significantly reduce gas porosity formation compared to gas atomized powders, as were used in this study [52,53]. However, the present study has demonstrated that these smaller pores tend to have relatively little impact on mechanical behavior and can therefore, for the most part, be ignored.

Additionally, it is hypothesized that the cause of the significant increase in distance to gage center of the largest pores is due to the path of the laser during part creation. It is well-established that keyhole porosity formation is due to excessive energy input in LPBF AM and similar processes such as laser welding [21,31,54]. Thus, it is hypothesized that the laser scan pattern used in the printing of the samples used in this study resulted in non-uniform energy density input, specifically a localized increase in spatial energy density near the sample edges. Figure 11 presents images of the same keyhole pore at different magnifications as seen from the processed CT volume. These images highlight both the location of the pore as close to the edge of the sample as well as the general shape of the defect.

Although the accuracy of shape descriptions of pores obtained from CT data are limited by the resolution of the scan, a well-documented limitation of CT porosity identification [55], it is believed that the pores of most consequence in this study, those >125 μm diameter, are assessed with an appropriate degree of accuracy. With ≥ 12 voxels in diameter, shape descriptors, particularly those that are PCAx-related, are hypothesized to be adequately obtained. Other measurements that may be more susceptible to resolution effects such as surface area may be more impacted. However, the porosity detection algorithm used in the present study is capable of inter-voxel interpolation which can increase porosity detection to sub-voxel resolution [56]. However, shape assessment on smaller pores are likely much less accurate. More thorough shape characterization for these pores would require instrumentation with capabilities beyond that of standard laboratory CT sources, which are typically only capable of only down to ~5 μm resolution [42]. Use of these higher resolution systems can significantly limit inspectable sample size [30] and make inspections of many samples such as the 75 inspected in this study impractical.

As has been well-established that in AM metals such as aluminum and titanium, keyhole pore formation at the end of laser tracks is significantly more likely than in the steady-state regions in the middle of the laser tracks [28,57]. The resulting pores are sometimes referred to as end-of-track (EoT) pores. The occurrence of keyhole pores has been shown to increase with energy density due to keyhole fluctuation [57]. The results of the present study suggest that even higher GED input would result in keyhole porosity forming not only at the edges of samples but in the center of these samples as well, resulting in further reduction of tensile properties. Ref. [28] suggests that because of the increased likelihood of porosity formation in the EoT region, optimization of processing conditions such as laser power and energy density could be used to mitigate these issues. Although dynamic control of laser parameters is not yet available on most commercial AM machines, researchers at NIST have developed a custom AM system that allows for this dynamic, granular control of scanning parameters [58].

With this level of control not yet widely available, others have turned to re-melting or repair strategies to remove such EoT pores. An example of a re-melting strategy is the contour strategy employed as part of the default EOS parameters used for the printing of parts used in this study. However, Kiss et al. [59] demonstrated, albeit in Ti64, that such repair strategies either failed to remove pores or formed more pores during the repair, concluding that laser re-melting techniques are impractical as void repair strategies. As such, the pores near the edge of samples in the present study are practically inevitable at the current stage of technology widely available, even with the implemented contour scanning strategy. It is anticipated, though the referenced study was conducted on a different material system, that the fundamental physics will stay the same and therefore present similar difficulties for 316L.

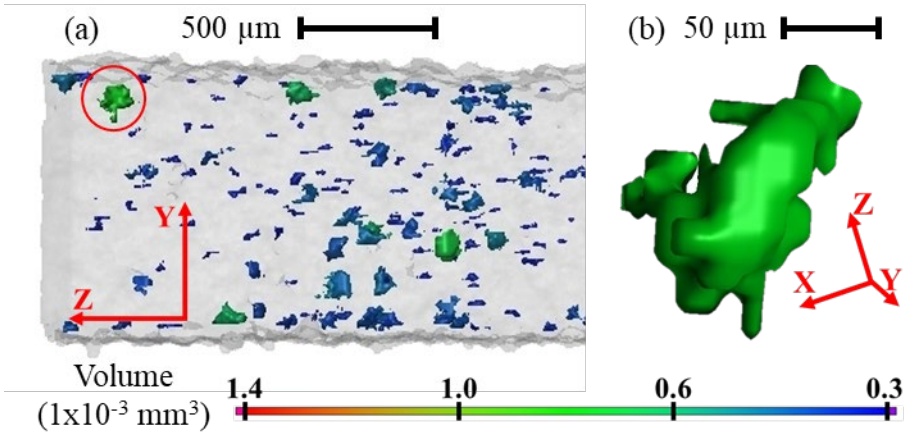

Figure 11. Example of keyhole porosity in high GED sample showing shape and distance from center shown at different magnifications and perspectives. Defect color indicates pore volume ($1x10^3$ mm^3) as shown on scale bar.

4.2 Qualification Implications

Porosity has long been suspected to be detrimental to tensile performance, yet its exact effects remain elusive. The results presented in this study suggest that internal defects can be used as one metric in AM component qualification. This is significant for the AM community because with the initial understanding of the relationship between porosity and tensile performance established in this study, parts may be able to be qualified for use without testing many specific components to establish inspection metrics on a component-by-component basis. This indicates that statistical models of the defect-property relationship could be used to save significant amounts of time on money spent on qualifying a re-designed part.

Perhaps the most significant finding of the results presented above is that it may be possible to predict global part performance using only the largest pores in a sample. The present study found that pores above 125 µm diameter have the most significant effect on tensile performance. For comparison, the American Welding Society (AWS) additive manufacturing standard, AWS D20.1/20.1M [34], and AWS fusion welding standard, AWS D17.1/17.1M:2017—AMD2 [35], allow critical application components to contain sub-surface pores of up to 0.33 times the thickness (330 µm pores in the parts used in this study) or 1.5 mm diameter for larger parts. In light of the significant variability in part performance observed in the present study along with the correlation between larger pores and global tensile performance, these standards may not be strict enough. If pores ≥125 µm are all that need to be detected, it is feasible that lower-resolution inspection methods for performance predictions may be adequate as inspection tools. Alternatively, high-grade CT systems may be used for higher inspection confidence and probability of detection.

Results presented in this study are consistent with other studies such as that by Madison et al. [9] and Kramer et al. [2] in the conclusion that porosity impacts tensile performance of additively manufactured components. Ref. [9], investigating 17-4PH SS, found that maximum R^2 values of approximately 0.50 exist for correlation of porosity characteristics and tensile performance. These results, despite being performed on a different material system, are very similar to results in this study. The present study, however, found that consideration of only the largest pores can significantly improve the R^2 values of these relationships. Ref. [2], investigating 316L SS, found

that cracks initiate sooner and grow more quickly because of porosity. It also found that porosity affected fracture path significantly. This early initiation of cracks by large voids identified in Ref. [2] is consistent with the low elongation properties seen in the samples of the present study. Ref. [2] did not investigate the strength of these relationships through R^2 analysis, but concluded that an obvious relationship between voids and mechanical behavior remained elusive. The similar conclusions of the referenced study to those of the present study lend legitimacy to the correlations presented and provide further understanding of the reasons for low elongation values in samples with large porosity from a fracture mechanics perspective.

Furthermore, both ductility and strain at UTS were shown to be negatively impacted by porosity, as measured by volume and other characteristics. This is important because 316L SS is often chosen for its ductile material response and ability to absorb energy. Elastic modulus, UTS, and yield stress and strain were all shown to be fairly constant across all GED conditions and only moderately correlated with porosity characteristics. This is consistent with the findings of others and shows that porosity needs relatively little consideration when designing components that will only experience elastic loading conditions.

Lastly, little to no correlation was seen between pore shape and global tensile performance. It is suspected that pore shape may have impact on local tensile behavior or under fatigue loading conditions where defect shape often is more significant. However, as mentioned above, higher-resolution equipment and smaller sample sizes would be necessary to detect these small pores and assess pore shape with higher accuracy. While other variables (e.g., microstructure, surface roughness, surface defects) may also influence mechanical properties, the present work has highlighted clear correlations between the above porosity characteristics and global mechanical properties. Future studies that can control for these other variables through heat treatment microstructure normalization or post-processing to mitigate surface effects may reveal further insights into the role of porosity in global tensile performance.

5 Conclusions

The present work focused on developing an understanding of the role of internal porosity defects created by variations in spatial energy distributions on global tensile performance of 316L SS samples to address the current lack of thorough understanding of this relationship. This study developed an improved understanding of this relationship through correlation of porosity features and mechanical properties and is useful for the development of inspection standards for critical structural components such as those in aerospace and defense. The major conclusions of this study are:

1. The largest defects (those in excess of 125 μm diameter) in a sample have the largest impact on global tensile behavior.
2. Defect size, as measured by volume, is the most significant characteristic, of those investigated, that is correlated with tensile behavior.
3. Ductility and strain at ultimate tensile strength are the global tensile properties most significantly negatively impacted by porosity.
4. UTS, elastic modulus, yield stress, and yield strain were not shown to be affected by porosity characteristics.
5. Pore shape demonstrated little effect on tensile properties.

Acknowledgements

This work was supported in part by the Department of Energy [DE-EE0008303] and the National Science Foundation [CMMI-1646013, CMMI-1825640 and IIP-1631803]. Sandia National Laboratories is a multimission laboratory managed and operated by National Technology & Engineering Solutions of Sandia, LLC, a wholly owned subsidiary of Honeywell International Inc., for the U.S. Department of Energy's National Nuclear Security Administration under contract DE-NA0003525. This paper describes objective technical results and analysis. Any subjective views or opinions that might be expressed in the paper do not necessarily represent the views of the U.S. Department of Energy or the United States Government.

Declaration of Interest

The authors declare that they have no known competing financial interests or personal relationships that could have appeared to influence the work reported in this paper.

CRediT Authorship Contribution Statement

Elliott Jost: Conceptualization, data curation, investigation, formal analysis, methodology, software, writing - original draft, writing – review & editing; **John Miers:** Software, investigation**,** writing – review & editing; **Aron Robbins:** Investigation, writing – review & editing; **David Moore:** Resources, supervision, funding acquisition, writing – review & editing; **Christopher Saldana:** Resources, supervision, funding acquisition, project administration, writing – review & editing

References

[1] M. Seifi, M. Gorelik, J. Waller, N. Hrabe, N. Shamsaei, S. Daniewicz, J.J. Lewandowski, Progress Towards Metal Additive Manufacturing Standardization to Support Qualification and Certification, JOM. 69 (2017) 439–455. https://doi.org/10.1007/s11837-017-2265-2.

[2] S.L.B. Kramer, T.A. Ivanoff, J.D. Madison, A.P. Lentfer, Evolution of Damage and Failure in an Additively Manufactured 316l SS Structure: Experimental Reinvestigation of the Third Sandia Fracture Challenge, Int J Fract. (2019). https://doi.org/10.1007/s10704-019-00357-x.

[3] S. Shrestha, T. Starr, K. Chou, A Study of Pore Formation During Single Layer and Multiple Layer Build by Selective Laser Melting, in: Solid Freeform Fabrication 2019, Austin, TX, n.d.: p. 11.

[4] R. Cunningham, S.P. Narra, C. Montgomery, J. Beuth, A.D. Rollett, Synchrotron-Based X-ray Microtomography Characterization of the Effect of Processing Variables on Porosity Formation in Laser Power-Bed Additive Manufacturing of Ti-6Al-4V, JOM. 69 (2017) 479–484. https://doi.org/10.1007/s11837-016-2234-1.

[5] R. Cunningham, S.P. Narra, T. Ozturk, J. Beuth, A.D. Rollett, Evaluating the Effect of Processing Parameters on Porosity in Electron Beam Melted Ti-6Al-4V via Synchrotron X-ray Microtomography, JOM. 68 (2016) 765–771. https://doi.org/10.1007/s11837-015-1802-0.

[6] V. Aloisi, S. Carmignato, Influence of Surface Roughness on X-Ray Computed Tomography Dimensional Measurements of Additive Manufactured Parts, Case Studies in Nondestructive Testing and Evaluation. 6 (2016) 104–110. https://doi.org/10.1016/j.csndt.2016.05.005.

[7] H. Gong, K. Rafi, H. Gu, G.D. Janaki Ram, T. Starr, B. Stucker, Influence of Defects on Mechanical Properties of Ti–6Al–4V Components Produced by Selective Laser Melting and Electron Beam Melting, Materials & Design. 86 (2015) 545–554. https://doi.org/10.1016/j.matdes.2015.07.147.
[8] H. Masuo, Y. Tanaka, S. Morokoshi, H. Yagura, T. Uchida, Y. Yamamoto, Y. Murakami, Influence of Defects, Surface Roughness and Hip on the Fatigue Strength of Ti-6Al-4V Manufactured by Additive Manufacturing, International Journal of Fatigue. 117 (2018) 163–179. https://doi.org/10.1016/j.ijfatigue.2018.07.020.
[9] J.D. Madison, O.D. Underwood, L.P. Swiler, B.L. Boyce, B.H. Jared, J.M. Rodelas, B.C. Salzbrenner, Corroborating tomographic defect metrics with mechanical response in an additively manufactured precipitation-hardened stainless steel, in: Provo, Utah, USA, 2018: p. 020009. https://doi.org/10.1063/1.5031506.
[10] J.A. Slotwinski, E.J. Garboczi, Metrology Needs for Metal Additive Manufacturing Powders, JOM. 67 (2015) 538–543. https://doi.org/10.1007/s11837-014-1290-7.
[11] F.H. Kim, S.P. Moylan, Literature Review of Metal Additive Manufacturing Defects, National Institute of Standards and Technology, Gaithersburg, MD, 2018. https://doi.org/10.6028/NIST.AMS.100-16.
[12] B. Cheng, J. Lydon, K. Cooper, V. Cole, P. Northrop, K. Chou, Melt Pool Dimension Measurement In Selective Laser Melting Using Thermal Imaging, in: Solid Freeform Fabrication 2017, Austin, TX, n.d.: p. 12.
[13] T.G. Spears, S.A. Gold, In-Process Sensing in Selective Laser Melting (SLM) Additive Manufacturing, Integrating Materials and Manufacturing Innovation. 5 (2016). https://doi.org/10.1186/s40192-016-0045-4.
[14] R.K. Leach, D. Bourell, S. Carmignato, A. Donmez, N. Senin, W. Dewulf, Geometrical Metrology for Metal Additive Manufacturing, CIRP Annals. 68 (2019) 677–700. https://doi.org/10.1016/j.cirp.2019.05.004.
[15] M. Seifi, A. Salem, J. Beuth, O. Harrysson, J.J. Lewandowski, Overview of Materials Qualification Needs for Metal Additive Manufacturing, JOM. 68 (2016) 747–764. https://doi.org/10.1007/s11837-015-1810-0.
[16] M. Seifi, A. Salem, D. Satko, J. Shaffer, J.J. Lewandowski, Defect distribution and microstructure heterogeneity effects on fracture resistance and fatigue behavior of EBM Ti–6Al–4V, International Journal of Fatigue. 94 (2017) 263–287. https://doi.org/10.1016/j.ijfatigue.2016.06.001.
[17] B.L. Boyce, B.C. Salzbrenner, J.M. Rodelas, L.P. Swiler, J.D. Madison, B.H. Jared, Y.-L. Shen, Extreme-Value Statistics Reveal Rare Failure-Critical Defects in Additive Manufacturing: Extreme-Value Statistics Reveal Rare Failure- Critical Defects…, Advanced Engineering Materials. 19 (2017) 1700102. https://doi.org/10.1002/adem.201700102.
[18] H.D. Carlton, K.D. Klein, J.W. Elmer, Evolution of microstructure and mechanical properties of selective laser melted Ti-5Al-5V-5Mo-3Cr after heat treatments, Science and Technology of Welding and Joining. (2019) 1–9. https://doi.org/10.1080/13621718.2019.1594589.
[19] H.D. Carlton, A. Haboub, G.F. Gallegos, D.Y. Parkinson, A.A. MacDowell, Damage Evolution and Failure Mechanisms in Additively Manufactured Stainless Steel, Materials Science and Engineering: A. 651 (2016) 406–414. https://doi.org/10.1016/j.msea.2015.10.073.

[20] J.-B. Forien, N.P. Calta, P.J. DePond, G.M. Guss, T.T. Roehling, M.J. Matthews, Detecting keyhole pore defects and monitoring process signatures during laser powder bed fusion: a correlation between in situ pyrometry and ex situ X-ray radiography, Additive Manufacturing. (2020) 101336. https://doi.org/10.1016/j.addma.2020.101336.
[21] W.E. King, Observation of Keyhole-Mode Laser Melting in Laser Powder-Bed Fusion Additive Manufacturing, Journal of Materials Processing Technology. (2014) 11.
[22] T. Ronneberg, C.M. Davies, P.A. Hooper, Revealing relationships between porosity, microstructure and mechanical properties of laser powder bed fusion 316L stainless steel through heat treatment, Materials & Design. 189 (2020) 108481. https://doi.org/10.1016/j.matdes.2020.108481.
[23] A.E. Wilson-Heid, T.C. Novak, A.M. Beese, Characterization of the Effects of Internal Pores on Tensile Properties of Additively Manufactured Austenitic Stainless Steel 316L, Experimental Mechanics. 59 (2019) 793–804. https://doi.org/10.1007/s11340-018-00465-0.
[24] G. Ziółkowski, E. Chlebus, P. Szymczyk, J. Kurzac, Application of X-ray CT method for discontinuity and porosity detection in 316L stainless steel parts produced with SLM technology, Archives of Civil and Mechanical Engineering. 14 (2014) 608–614. https://doi.org/10.1016/j.acme.2014.02.003.
[25] M. Grasso, V. Laguzza, Q. Semeraro, B.M. Colosimo, In-Process Monitoring of Selective Laser Melting: Spatial Detection of Defects Via Image Data Analysis, Journal of Manufacturing Science and Engineering. 139 (2016) 051001. https://doi.org/10.1115/1.4034715.
[26] H. Gaja, F. Liou, Defects Classification of Laser Metal Deposition Using Acoustic Emission Sensor, in: Solid Freeform Fabrication 2017, Austin, TX, n.d.: p. 13.
[27] C.L.A. Leung, S. Marussi, R.C. Atwood, M. Towrie, P.J. Withers, P.D. Lee, In Situ X-Ray Imaging of Defect and Molten Pool Dynamics in Laser Additive Manufacturing, Nature Communications. 9 (2018). https://doi.org/10.1038/s41467-018-03734-7.
[28] A.A. Martin, N.P. Calta, J.A. Hammons, S.A. Khairallah, M.H. Nielsen, R.M. Shuttlesworth, N. Sinclair, M.J. Matthews, J.R. Jeffries, T.M. Willey, J.R.I. Lee, Ultrafast Dynamics of Laser-Metal Interactions in Additive Manufacturing Alloys Captured by in Situ X-Ray Imaging, Materials Today Advances. 1 (2019) 100002. https://doi.org/10.1016/j.mtadv.2019.01.001.
[29] F.H. Kim, S.P. Moylan, E.J. Garboczi, J.A. Slotwinski, Investigation of pore structure in cobalt chrome additively manufactured parts using X-ray computed tomography and three-dimensional image analysis, Additive Manufacturing. 17 (2017) 23–38. https://doi.org/10.1016/j.addma.2017.06.011.
[30] E. Maire, P.J. Withers, Quantitative X-ray tomography, International Materials Reviews. 59 (2014) 1–43. https://doi.org/10.1179/1743280413Y.0000000023.
[31] A.A. Martin, N.P. Calta, S.A. Khairallah, J. Wang, P.J. Depond, A.Y. Fong, V. Thampy, G.M. Guss, A.M. Kiss, K.H. Stone, C.J. Tassone, J. Nelson Weker, M.F. Toney, T. van Buuren, M.J. Matthews, Dynamics of Pore Formation During Laser Powder Bed Fusion Additive Manufacturing, Nat Commun. 10 (2019) 1987. https://doi.org/10.1038/s41467-019-10009-2.
[32] T. DebRoy, H.L. Wei, J.S. Zuback, T. Mukherjee, J.W. Elmer, J.O. Milewski, A.M. Beese, A. Wilson-Heid, A. De, W. Zhang, Additive manufacturing of metallic components – Process, structure and properties, Progress in Materials Science. 92 (2018) 112–224. https://doi.org/10.1016/j.pmatsci.2017.10.001.

[33] T. Mukherjee, T. DebRoy, Mitigation of Lack of Fusion Defects in Powder Bed Fusion Additive Manufacturing, Journal of Manufacturing Processes. 36 (2018) 442–449. https://doi.org/10.1016/j.jmapro.2018.10.028.
[34] American Welding Society, D20 Committee on Additive Manufacturing, American Welding Society, Technical Activities Committee, American National Standards Institute, Specification for fabrication of metal components using additive manufacturing, 2019.
[35] American National Standards Institute, American Welding Society, D17 Committee on Welding in the Aircraft and Aerospace Industries, American Welding Society, Technical Activities Committee, Specification for fusion welding for aerospace applications, 2018.
[36] Z. Dong, Y. Liu, W. Li, J. Liang, Orientation dependency for microstructure, geometric accuracy and mechanical properties of selective laser melting AlSi10Mg lattices, Journal of Alloys and Compounds. 791 (2019) 490–500. https://doi.org/10.1016/j.jallcom.2019.03.344.
[37] R. Wauthle, B. Vrancken, B. Beynaerts, K. Jorissen, J. Schrooten, J.-P. Kruth, J. Van Humbeeck, Effects of Build Orientation and Heat Treatment on the Microstructure and Mechanical Properties of Selective Laser Melted Ti6al4v Lattice Structures, Additive Manufacturing. 5 (2015) 77–84. https://doi.org/10.1016/j.addma.2014.12.008.
[38] A.D. Dressler, E.W. Jost, J.C. Miers, D.G. Moore, C.C. Seepersad, B.L. Boyce, Heterogeneities dominate mechanical performance of additively manufactured metal lattice struts, Additive Manufacturing. 28 (2019) 692–703. https://doi.org/10.1016/j.addma.2019.06.011.
[39] S. Ghouse, S. Babu, K. Nai, P.A. Hooper, J.R.T. Jeffers, The influence of laser parameters, scanning strategies and material on the fatigue strength of a stochastic porous structure, Additive Manufacturing. 22 (2018) 290–301. https://doi.org/10.1016/j.addma.2018.05.024.
[40] K. Guan, Z. Wang, M. Gao, X. Li, X. Zeng, Effects of processing parameters on tensile properties of selective laser melted 304 stainless steel, Materials & Design. 50 (2013) 581–586. https://doi.org/10.1016/j.matdes.2013.03.056.
[41] E28 Committee, Test Methods for Tension Testing of Metallic Materials, ASTM International, n.d. https://doi.org/10.1520/E0008_E0008M-11.
[42] A. du Plessis, I. Yadroitsev, I. Yadroitsava, S.G. Le Roux, X-Ray Microcomputed Tomography in Additive Manufacturing: A Review of the Current Technology and Applications, 3D Printing and Additive Manufacturing. 5 (2018) 227–247. https://doi.org/10.1089/3dp.2018.0060.
[43] A. du Plessis, P. Sperling, A. Beerlink, L. Tshabalala, S. Hoosain, N. Mathe, S.G. le Roux, Standard Method for Microct-Based Additive Manufacturing Quality Control 1: Porosity Analysis, MethodsX. 5 (2018) 1102–1110. https://doi.org/10.1016/j.mex.2018.09.005.
[44] S. Tammas-Williams, H. Zhao, F. Léonard, F. Derguti, I. Todd, P.B. Prangnell, XCT analysis of the influence of melt strategies on defect population in Ti–6Al–4V components manufactured by Selective Electron Beam Melting, Materials Characterization. 102 (2015) 47–61. https://doi.org/10.1016/j.matchar.2015.02.008.
[45] B.C. Salzbrenner, J.M. Rodelas, J.D. Madison, B.H. Jared, L.P. Swiler, Y.-L. Shen, B.L. Boyce, High-throughput stochastic tensile performance of additively manufactured stainless steel, Journal of Materials Processing Technology. 241 (2017) 1–12. https://doi.org/10.1016/j.jmatprotec.2016.10.023.
[46] ASM International, ed., ASM Handbook: Properties and Selection: Irons, Steels, and High-Performance Alloys, 10th editon, ASM International, Materials Park, Ohio, 1990.

[47] A.M. Roach, B.C. White, A. Garland, B.H. Jared, J.D. Carroll, B.L. Boyce, Size-Dependent Stochastic Tensile Properties in Additively Manufactured 316l Stainless Steel, Additive Manufacturing. 32 (2020) 101090. https://doi.org/10.1016/j.addma.2020.101090.
[48] T. Niendorf, S. Leuders, A. Riemer, H.A. Richard, T.T. Ster, D. Schwarze, Highly Anisotropic Steel Processed by Selective Laser Melting, Metallurgical and Materials Transactions B. 44 (2013) 794–796. https://doi.org/10.1007/s11663-013-9875-z.
[49] E. Garlea, H. Choo, C.C. Sluss, M.R. Koehler, R.L. Bridges, X. Xiao, Y. Ren, B.H. Jared, Variation of elastic mechanical properties with texture, porosity, and defect characteristics in laser powder bed fusion 316L stainless steel, Materials Science and Engineering: A. 763 (2019) 138032. https://doi.org/10.1016/j.msea.2019.138032.
[50] H.M. Ledbetter, Predicted single-crystal elastic constants of stainless-steel 316, British Journal of Non-Destructive Testing. 23 (1981) 286–287.
[51] Standard Test Method for Dynamic Young's Modulus, Shear Modulus, and Poisson's Ratio by Impulse Excitation of Vibration.
[52] M.N. Ahsan, A.J. Pinkerton, R.J. Moat, J. Shackleton, A comparative study of laser direct metal deposition characteristics using gas and plasma-atomized Ti–6Al–4V powders, Materials Science and Engineering: A. 528 (2011) 7648–7657. https://doi.org/10.1016/j.msea.2011.06.074.
[53] M.N. Ahsan, R. Bradley, A.J. Pinkerton, Microcomputed tomography analysis of intralayer porosity generation in laser direct metal deposition and its causes, Journal of Laser Applications. 23 (2011) 022009. https://doi.org/10.2351/1.3582311.
[54] J.D. Madison, L.K. Aagesen, Quantitative Characterization of Porosity in Laser Welds of Stainless Steel, Scripta Materialia. 67 (2012) 783–786. https://doi.org/10.1016/j.scriptamat.2012.06.015.
[55] A. Thompson, I. Maskery, R.K. Leach, X-Ray Computed Tomography for Additive Manufacturing: A Review, Measurement Science and Technology. 27 (2016) 072001. https://doi.org/10.1088/0957-0233/27/7/072001.
[56] J.P. Kruth, M. Bartscher, S. Carmignato, R. Schmitt, L. De Chiffre, A. Weckenmann, Computed Tomography for Dimensional Metrology, CIRP Annals. 60 (2011) 821–842. https://doi.org/10.1016/j.cirp.2011.05.006.
[57] S.M.H. Hojjatzadeh, Direct Observation of Pore Formation Mechanisms During LPBF Additive Manufacturing Process and High Energy Density Laser Welding, International Journal of Machine Tools and Manufacture. (2020) 8.
[58] H. Yeung, B. Lane, J. Fox, Part Geometry and Conduction-Based Laser Power Control for Powder Bed Fusion Additive Manufacturing, Additive Manufacturing. 30 (2019) 100844. https://doi.org/10.1016/j.addma.2019.100844.
[59] A.M. Kiss, Laser-Induced Keyhole Defect Dynamics during Metal Additive Manufacturing, Adv. Eng. Mater. (2019) 7.